



# Kent Academic Repository

Caddeo, Francesco, Casu, Alberto, Loche, Danilo, Morgan, Lucy M., Mountjoy, Gavin, O'Regan, Colm, Casula, Maria F., Hayama, Shusaku, Corrias, Anna and Falqui, Andrea (2021) *Thermally Stable Surfactant-Free Ceria Nanocubes in Silica Aerogel*. *Journal of Colloids and Interface Science*, 583 . pp. 376-384. ISSN 0021-9797.

## Downloaded from

<https://kar.kent.ac.uk/82981/> The University of Kent's Academic Repository KAR

## The version of record is available from

<https://doi.org/10.1016/j.jcis.2020.09.044>

## This document version

Publisher pdf

## DOI for this version

## Licence for this version

CC BY (Attribution)

## Additional information

## Versions of research works

### Versions of Record

If this version is the version of record, it is the same as the published version available on the publisher's web site. Cite as the published version.

### Author Accepted Manuscripts

If this document is identified as the Author Accepted Manuscript it is the version after peer review but before type setting, copy editing or publisher branding. Cite as Surname, Initial. (Year) 'Title of article'. To be published in *Title of Journal*, Volume and issue numbers [peer-reviewed accepted version]. Available at: DOI or URL (Accessed: date).

## Enquiries

If you have questions about this document contact [ResearchSupport@kent.ac.uk](mailto:ResearchSupport@kent.ac.uk). Please include the URL of the record in KAR. If you believe that your, or a third party's rights have been compromised through this document please see our [Take Down policy](https://www.kent.ac.uk/guides/kar-the-kent-academic-repository#policies) (available from <https://www.kent.ac.uk/guides/kar-the-kent-academic-repository#policies>).



Contents lists available at ScienceDirect

## Journal of Colloid and Interface Science

journal homepage: [www.elsevier.com/locate/jcis](http://www.elsevier.com/locate/jcis)

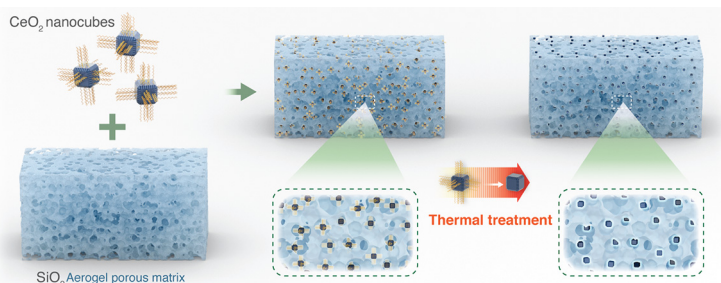
## Regular Article

## Thermally stable surfactant-free ceria nanocubes in silica aerogel

Francesco Caddeo<sup>a,1</sup>, Alberto Casu<sup>b,1</sup>, Danilo Loche<sup>a,1</sup>, Lucy M. Morgan<sup>a</sup>, Gavin Mountjoy<sup>a</sup>, Colm O'Regan<sup>b</sup>, Maria F. Casula<sup>c</sup>, Shusaku Hayama<sup>d</sup>, Anna Corrias<sup>a,\*</sup>, Andrea Falqui<sup>b,\*</sup>

<sup>a</sup> School of Physical Sciences, Ingram Building, University of Kent, Canterbury CT2 7NH, United Kingdom<sup>b</sup> King Abdullah University of Science and Technology (KAUST), Biological and Environmental Sciences and Engineering (BESE) Division, Nabla Lab, 23955-6900 Thuwal, Saudi Arabia<sup>c</sup> Department of Mechanical, Chemical and Material Engineering, University of Cagliari, via Marengo 2, I-09123 Cagliari, Italy<sup>d</sup> Diamond Light Source, Harwell Science & Innovation Campus, Didcot OX11 0DE, United Kingdom

## GRAPHICAL ABSTRACT



## ARTICLE INFO

## Article history:

Received 3 August 2020

Revised 1 September 2020

Accepted 12 September 2020

Available online 22 September 2020

## Keywords:

Ceria  
Nanocubes  
Capping agents  
SiO<sub>2</sub> Aerogel

## ABSTRACT

Surfactant-mediated chemical routes allow one to synthesize highly engineered shape- and size-controlled nanocrystals. However, the occurrence of capping agents on the surface of the nanocrystals is undesirable for selected applications. Here, a novel approach to the production of shape-controlled nanocrystals which exhibit high thermal stability is demonstrated. Ceria nanocubes obtained by surfactant-mediated synthesis are embedded inside a highly porous silica aerogel and thermally treated to remove the capping agent. Powder X-ray Diffraction and Scanning Transmission Electron Microscopy show the homogeneous dispersion of the nanocubes within the aerogel matrix. Remarkably, both the size and the shape of the ceria nanocubes are retained not only throughout the aerogel syntheses but also upon thermal treatments up to 900 °C, while avoiding their agglomeration. The reactivity of ceria is measured by *in situ* High-Energy Resolution Fluorescence Detected - X-ray Absorption Near Edge Spectroscopy at the Ce L<sub>3</sub> edge, and shows the reversibility of redox cycles of ceria nanocubes when they are embedded in the aerogel. This demonstrates that the enhanced reactivity due to their prominent {100} crystal facets is preserved. In contrast, unsupported ceria nanocubes begin to agglomerate as soon as the capping agent decomposes, leading to a degradation of their reactivity already at 275 °C.

© 2020 The Authors. Published by Elsevier Inc. This is an open access article under the CC BY license (<http://creativecommons.org/licenses/by/4.0/>).

\* Corresponding authors.

E-mail addresses: [a.corrias@kent.ac.uk](mailto:a.corrias@kent.ac.uk) (A. Corrias), [andrea.falqui@kaust.edu.sa](mailto:andrea.falqui@kaust.edu.sa) (A. Falqui).

<sup>1</sup> These authors contributed equally.<https://doi.org/10.1016/j.jcis.2020.09.044>

0021-9797/© 2020 The Authors. Published by Elsevier Inc.

This is an open access article under the CC BY license (<http://creativecommons.org/licenses/by/4.0/>).

## 1. Introduction

The application of nanocrystals to critical areas such as biomedicine, environment, and energy requires careful design of chemical composition, crystal structure, surface coverage, size, and shape of the nanocrystals. Great efforts have been devoted to the devel-

opment of synthetic routes for the preparation of crystalline nanoparticles (NPs) with well-defined morphology, where the best results have so far been achieved by surfactant-assisted high temperature thermal decomposition of inorganic precursors in solution [1–3]. It is acknowledged that in this approach surfactants play a key role, as they mediate nucleation and growth of the NPs and are able to determine the final shape by selective or preferential adhesion to specific crystal seed facets. Eventually, surfactants will be present on the surface of NPs as capping agents, preventing their agglomeration and growth, determining dispersibility in desired solvents or providing surface functionality. Surfactant-mediated hydro-solvothermal methods have also been developed due to their potential for scaling up of synthetic protocols, and have been demonstrated to be very successful especially for the morphology-controlled synthesis of oxides [4–6]. So far surfactant-assisted chemical approaches have been successfully used for the production of plasmonic, magnetic, semiconducting, and fluorescent NPs with highly precisely selected nearly monodisperse size and shape [7–15].

While the surface coverage of surfactant-capped NPs can be exploited to provide additional functionality, thus enabling their use in areas such as biosensing, it is also well-known that surfactants might limit applications in other technologically relevant fields such as catalysis [16]. First of all, the NPs are usually obtained as colloidal dispersions, and although they can be isolated from the dispersing media, the resulting powders are difficult to handle for solid-state applications. Most importantly, the occurrence of capping agents might limit access to the NP surfaces as well as have a detrimental effect on transport phenomena involved in the catalytic process. Finally, capped NPs might not be suitable for applications requiring high operating temperatures which would result in degradation of the capping agent, leading to NP agglomeration, with a consequent loss of control over shape and size-dependent properties, and with a dramatic reduction of the effective specific surface area and of the related reactivity. The removal of capping ligands is indeed acknowledged as a major challenge for the design of effective catalysts, and this issue has been investigated for metal-based catalysts through nanoparticle deposition over a solid substrate followed by either washing with hot solvents or acidic solutions, or UV-Ozone irradiation, or very rapid reactive thermal treatment [17–20].

A relevant goal to extend the application of NPs is hence to develop strategies which enable surfactant removal while retaining properties associated with their controlled shape. This is particularly relevant for ceria (i.e. cerium (IV) oxide), which plays a key role in many fields including catalysis, biomedicine, and environmental remediation [21–23]. Ceria has been obtained in form of morphology-controlled NPs by surfactant-assisted routes, and is widely used and investigated as a catalyst on both industrial and research scale [24], owing to its high potential for a range of catalytic processes of paramount importance, including steam methane reforming [25], CO oxidation [26,27], soot oxidation [28,29], water gas shift reaction [30–32], and hydrogenation reactions [33,34]. The unique properties of ceria relate to its ability to store and release oxygen from the crystal lattice, via the reversible formation of oxygen vacancies, which act as active sites during the catalytic processes [35]. This property is associated with the distinctive ability of cerium ions to undergo transition between Ce (III) and Ce(IV) oxidation states [36] which is quantified in terms of Oxygen Storage Capacity (OSC), defined as  $\mu\text{mol}$  of oxygen atoms released and stored per gram of ceria during a complete redox cycle [37]. The amount of surface oxygen vacancies in ceria can be engineered by tuning the oxygen partial pressure of the environment [38]. Notably, the OSC and hence reactivity of ceria nanoparticles can be varied by controlling the crystal morphology,

due to the different tendency of specific crystal surfaces to form oxygen vacancies [39–41].

Ceria nanocubes (NCs) have shown the highest values of OSC, when compared to nanorods and irregularly shaped nanoparticles [42,43]. Thus, ceria NCs display the best potential as redox catalysts, since they expose on their surface six highly reactive {100} facets [44]. Successful strategies to produce  $\text{CeO}_2$  NCs rely on the use of fatty acids such as oleic acid, which binds preferentially to the {100} crystal facets, thus promoting a shape-selective synthesis [45,46]. This surfactant-assisted production also makes it possible to control and prevent excessive growth of the ceria NCs, a key requirement to produce them with small sizes in order to enhance catalytic performance, as calculations show that the energy required to form an oxygen vacancy is strongly dependent on the size of the NPs [47,48]. In this framework, Huebner et al. [49] found that ceria NPs with crystal size of 4 nm show a concentration of oxygen vacancies which is two orders of magnitude higher compared to NPs of 60 nm.

The shape dependence of  $\text{CeO}_2$  OSC was recently investigated by Cabot and co-workers by comparing branched and quasi-spherical NPs [50]. The role of a high surface-to-volume ratio in nanocrystals, and the possibility of retaining high surface area by assembling NPs into a porous three-dimensional (3D) solid, was also investigated. In particular, a 3D porous solid where  $\text{CeO}_2$  nanocrystals with well-controlled morphology retain their original features was obtained through surface modification routes, leading first to a gel structure and then to a porous solid in the form of aerogel by gel drying under supercritical conditions [51]. The proposed strategy addresses the issue of producing a 3D porous solid where the  $\text{CeO}_2$  NPs with well-controlled morphology retain their original features. Although a major limitation of this approach is that surface processing is required and surface modifiers are retained in the aerogel, the work by Cabot and co-workers has pointed out the potential of aerogels in the design of ceria-based solids with high porosity.

In this work, we provide a significant advance in the production of surfactant-free morphology-controlled  $\text{CeO}_2$  NCs through their stabilization into a highly porous silica aerogel, a well-known solid with remarkable ultra-low apparent density, high porosity, large specific surface area, and low thermal conductivity, which can be obtained in different forms including monoliths [52,53]. Its unique skeletal and surface properties [54] make silica aerogel an effective material in a very wide range of applications, including adsorption of organic pollutants [55], drug delivery [56], thermal insulation [57], and as a catalytic support [53,58]. Indeed, nanocomposites based on silica aerogels have already been demonstrated to act as heterogeneous catalysts with high chemical and thermal stability during diverse catalytic processes [59–61]. Aerogel nanocomposite catalysts produced by routine sol-gel strategies, however, do not allow tailoring of the size and shape of the catalytically active dispersed nanophase. Indeed, it should be noted that the literature on using porous materials as the substrate to disperse nanomaterials is extensive (references [59–61] being just an example). However, porous materials have not been used so far for the dispersion of shape and size controlled nanoparticles because of the challenges of combining the chemistry of colloids, needed for size and shape control, with the chemistry used to synthesize the porous materials, and their characteristics. Among porous materials aerogel catalysts show much higher activity and selectivity in various catalytic reactions, accompanied by remarkable stability [62]. For this reason a silica aerogel has been chosen as a porous support to stabilize  $\text{CeO}_2$  NCs.

Here, for the first time we show that we are able to produce highly porous solids made out of surfactant-free  $\text{CeO}_2$  NCs smaller than 10 nm average size, i.e. where both shape and size are

optimized for maximum reactivity, dispersed within the highly porous matrix of a SiO<sub>2</sub> aerogel. These nanocomposites are synthesized by loading pre-formed CeO<sub>2</sub> NCs during a modified sol-gel method to produce the silica aerogel which acts as a matrix/support. We then demonstrate that ceria NCs are still stable when submitted to thermal treatments up to 900 °C for 1 h because they are embedded in the silica aerogel, which not only gives rise to such a significant enhancement in terms of thermal stability, but also allows retention of their initial size and cubic shape.

To demonstrate the effectiveness of our method we have used a multi-technique approach, combining powder X-ray Diffraction (XRD), High Resolution Scanning Transmission Electron Microscopy (HRSTEM), and High-Energy Resolution Fluorescence Detected (HERFD) - X-ray Absorption Near Edge Spectroscopy (XANES) at the Ce L<sub>3</sub> edge. By combining XRD and advanced electron microscopy techniques we have been able to obtain information on the shape and size of ceria nanoparticles before and after embedding in the silica aerogel, as well as on the homogeneity of their distribution. We have then measured the reactivity of ceria by collecting high resolution XANES spectra *in situ* while cycling the samples at increasing temperatures, under reducing and oxidizing atmospheres. The latter technique is indeed able to accurately measure the amount of Ce<sup>3+</sup> and Ce<sup>4+</sup> in the samples, i.e. their OSC which is due to surface oxygen vacancies formed and filled during a redox cycle. Our results demonstrate the reversibility of the Ce<sup>3+</sup>/Ce<sup>4+</sup> equilibrium when the surfactant free ceria NCs are embedded in the silica aerogels.

## 2. Experimental

### 2.1. Synthesis of ceria nanocubes

The synthesis of the unsupported ceria NCs is reported in detail by Yang [46] and Loche [63]. Briefly, Ce(NO<sub>3</sub>)<sub>3</sub>·6H<sub>2</sub>O water solution, toluene, oleic acid and *tert*-butylamine are placed in an autoclave and the hydro-solvothermal synthesis is performed at 180 °C for 48 h. A separation and purification process with absolute ethanol follows and the final solid precipitate is dried at room temperature. By this procedure, CeO<sub>2</sub> NCs with average edge size of about 6 nm are obtained, as shown in Fig. 1A.

### 2.2. Synthesis of CeO<sub>2</sub>-SiO<sub>2</sub> aerogel nanocomposites

The aerogel nanocomposite was prepared through a modified protocol previously used for the synthesis of silica-based aerogels [64,65]. 1.975 mL of the silica precursor, tetraethoxysilane (Si(OC<sub>2</sub>H<sub>5</sub>)<sub>4</sub>, TEOS, Aldrich, 98%), was added to a mixture containing 0.75 mL of absolute ethanol (EtOH, Fluka) and 0.993 mL of acidic hydrolyzing solution (nitric acid (HNO<sub>3</sub>, Carlo Erba, 65%) in absolute ethanol and distilled water). 1 mL of a dispersion of ceria NCs in toluene, varying the concentration in order to obtain aerogel nanocomposites with 2 wt% and 6 wt% of ceria NCs, was then added to the TEOS-containing mixture, followed by adding a hydro-alcoholic solution of urea (NH<sub>2</sub>CONH<sub>2</sub>, Aldrich, >99.0%) under reflux at 85 °C. It was observed that the amount of toluene-based dispersion of capped CeO<sub>2</sub> NCs has to be optimized in order to promote undisturbed formation of silica gel. In fact, a progressive loss of the high porosity and low density characteristic of the aerogel matrix was observed when a large amount of toluene was used. We established the optimal toluene:ethanol ratio should not exceed 1:4 by volume. Within this limit, the typical porous structure of the aerogels is preserved in the final products, as demonstrated by N<sub>2</sub>-physisorption measurements reported in Fig. S1. The sol was kept in an oven at 40 °C until gelification and then submitted to high-temperature supercritical drying (up to

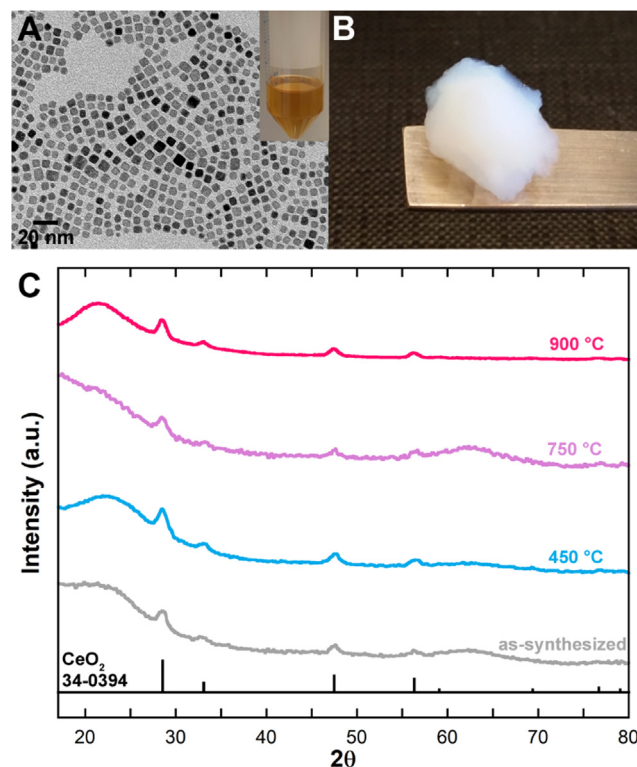


**Fig. 1.** (A) TEM image and visual appearance of the as-synthesized CeO<sub>2</sub> NCs; (B) Picture of the 2 wt% CeO<sub>2</sub>-SiO<sub>2</sub> aerogel nanocomposite; (C) XRD patterns of the 2 wt% CeO<sub>2</sub>-SiO<sub>2</sub> aerogel nanocomposite as-synthesized and treated at 450 °C, 750 °C and 900 °C.

330 °C, 70 atm) in an autoclave (Parr, 300 cm<sup>3</sup>) filled with 70 mL of absolute ethanol. The ceria wt% of the as-synthesized aerogel nanocomposites as determined by XRF analysis is reported in Table 1, showing that the effective amount of NCs dispersed in the silica matrix is quite close to that expected as a result of the performed synthesis. Fig. 1B shows the resulting 2 wt% CeO<sub>2</sub>-SiO<sub>2</sub> aerogel monolith, whose visual appearance suggests homogeneous distribution of ceria within the silica aerogel matrix.

### 2.3. Characterization

XRF analysis was carried out on a Panalytical Epsilon 3 Spectrometer.

Powder X-ray Diffraction (XRD) patterns were acquired in the 2θ range of 10° to 90° using a PANalytical X'Pert<sup>3</sup> diffractometer equipped with a Cu Kα line source and an X'Celerator linear detector. The Scherrer equation was applied for the calculation of the average size of crystallite domains, with application of a correction for instrumental broadening, determined with a LaB<sub>6</sub> standard.

Transmission Electron Microscopy (TEM) and spherical aberration (C<sub>s</sub>)-corrected High Resolution Scanning Transmission Electron Microscopy (C<sub>s</sub>-corrected HRSTEM) in High Angle Annular Dark Field (HAADF) geometry were performed using a double C<sub>s</sub>-corrected Thermo Fischer Scientific Titan Themis Cube microscope, equipped with a X-Twin objective lens, an ultra-bright field emission electron source (X-FEG), and working at an acceleration voltage of 300 kV, thus allowing an ultimate resolution of 0.7 Å.

High-Energy Resolution Fluorescence Detected (HERFD) - X-ray Absorption Near Edge Spectroscopy (XANES) data at the Ce L<sub>3</sub> edge were collected on unsupported CeO<sub>2</sub> NCs and on the NCs embedded in silica aerogel (aerogel nanocomposite containing 6 wt% NCs). Data were collected using a 1 m X-ray emission spectrometer

**Table 1**  
Nominal ceria loading in the two aerogel nanocomposites, and loading obtained by XRF.

Nominal loading (wt%)	XRF (wt%)
2	1.9 ± 0.1
6	5.7 ± 0.1

at the Diamond Light Source, on the I20 scanning beamline. For this experiment, the spectrometer was equipped with three Si (4,0,0) analyser crystals and a Si drift detector to observe the intensity of Ce  $L\alpha_1$  fluorescence line at 4840.2 eV. For each sample *in situ* oxidation (5% O<sub>2</sub> in He) and reduction (5% H<sub>2</sub> in He) cycles at 150 °C, 275 °C and 400 °C were performed, using a plug-flow reactor cell with Kapton tubes. The Kapton tube was filled with 1 cm of the NCs embedded in silica aerogel sample pushed to the centre of the tube, ensuring a homogeneous distribution of the sample in the beam. In the case of the unsupported NCs this was achieved using a toluene dispersion of CeO<sub>2</sub> NCs added to a small amount of quartz wool; once the toluene is evaporated off, the NCs impregnated in the quartz wool are placed in the centre of the tubes. Data were also collected on Ce<sup>4+</sup> and Ce<sup>3+</sup> reference compounds (CeO<sub>2</sub>, 99.9% Aldrich, and Ce(NO<sub>3</sub>)<sub>3</sub>·6H<sub>2</sub>O, 99.99% Aldrich) at room temperature. Data analysis was performed using the ATHENA software. The relative amounts of Ce<sup>3+</sup> and Ce<sup>4+</sup> was determined using the linear combination fitting tool in ATHENA [66].

FTIR spectra were collected on a Thermo Scientific Nicolet iS10 equipped with the ATR Smart iTR accessory and a DTGS (deuterated tri-glycine sulphate) detector.

N<sub>2</sub> adsorption-desorption measurements were carried out at 77 K on a Micromeritics ASAP2020 porosimeter. Prior to the analysis, the aerogels were outgassed at 473 K for 12 h, at a heating rate of 1 K·min<sup>-1</sup>.

### 3. Results and discussion

Ceria NCs have been produced by taking advantage of shape-selective surfactant-based hydrothermal procedures [46,63], which make use of oleic acid as a capping agent. Fig. 1A and S2 (A) show typical TEM images indicating the nearly monodisperse size and shape of the as-synthesized NCs. In particular, nanocubes with well-defined facets and edge sizes of about 6 nm are produced. TEM was also used to gain information on thermal stability of the capped NCs, providing clear evidence of agglomeration of the particles and loss of the cubic shape already after thermal treatment at 450 °C. Further thermal treatment at 750 °C leads to large ceria microcrystals (see Fig. S2(B) and (C)). These results are corroborated by the XRD patterns of the CeO<sub>2</sub> NCs, both as-synthesized and after thermal treatment at 450 °C and 750 °C, presented in Fig. S2(D). In fact, the XRD pattern of the as-synthesized CeO<sub>2</sub> NCs shows broad peaks due to the CeO<sub>2</sub> fluorite structure, with the typical preferential orientation due to the self-assembly of NCs, causing the {200} and {400} reflections to be the most intense. Conversely, in the XRD pattern obtained after thermal treatment at 450 °C, the peaks due to the CeO<sub>2</sub> fluorite structure show the typical intensity ratios expected in absence of preferential orientations [67] and are still broad, indicating that the agglomeration and concomitant loss of cubic shape is not yet accompanied by a considerable growth of the nanoparticle sizes. The same reflections and intensity ratios are present in the sample treated at 750 °C, but here the peaks appear much sharper, thus confirming that the formation of larger crystals has occurred.

The XRD patterns of the 2 wt% aerogel nanocomposite as-synthesized and treated at different temperatures are reported in Fig. 1C (see Fig. S3 for the XRD patterns of the 6 wt% aerogel

nanocomposites). The peaks corresponding to the fluorite crystalline structure of ceria can be identified [67] together with a broad halo around 24° arising from the contribution of the amorphous silica matrix. Remarkably, the XRD pattern of the aerogel nanocomposite does not show significant changes upon thermal treatment up to 900 °C. No evidence of additional phases is present. This indicates that cerium silicate phases, which were observed in silica-doped ceria [68], do not form.

FTIR spectroscopy analysis was used to gain insights into the fate of the capping agent throughout the production of the aerogel. In Fig. 2, the FTIR spectra (520–4000 cm<sup>-1</sup>) of the oleic acid (A) and ceria NCs (B), are compared with those of the 2 wt% aerogel nanocomposites as-synthesized (C) and thermally treated at 450 °C (D). As expected, the spectrum of the NCs confirms the presence of the surfactant, demonstrated by the typical bands of the oleic acid (–CH<sub>2</sub>– asymmetric and symmetric stretching at 2925–2854 cm<sup>-1</sup>, C=O stretching at 1711 cm<sup>-1</sup>, C–O–H bending at 1466–1412 cm<sup>-1</sup>, C–O stretching at 1284 cm<sup>-1</sup>). In the as-synthesized aerogel nanocomposite the bands of the oleic acid are still visible together with more pronounced bands of the silica (Si–O–Si stretching at 1071 cm<sup>-1</sup>, Si–OH stretching at 973 cm<sup>-1</sup>, Si–O–Si stretching at 798 cm<sup>-1</sup>). The bands of the oleic acid completely disappear after thermal treatment at 450 °C. These results show that oleic acid capping the ceria NCs is still present in the as-synthesized aerogel nanocomposite, indicating that the conditions used for supercritical drying (330 °C, inert atmosphere (N<sub>2</sub>)) prevent the degradation of the surfactant, which likely plays a role in the inhibition of ceria NCs agglomeration during the supercritical drying process. FTIR also demonstrates that the oleic acid is totally removed after the thermal treatment at 450 °C in air, as expected.

Hence, it is apparent that the aerogel matrix is able to stabilize the ceria NCs by preventing their agglomeration and consequent growth, even after the surfactant removal, in contrast to the case of the unsupported ceria NCs. This is indicated by both the intensity and width of the XRD peaks, which remain essentially unchanged up to 900 °C. Indeed, the ceria crystallite sizes in the aerogel nanocomposites, determined by the Scherrer equation to be 9 ± 1 nm, remain very similar to those of the unsupported original ceria NCs. This is a remarkable achievement considering industrial processes utilizing ceria are carried out at high temperature. However, XRD is not able to determine whether the ceria NPs maintain the cubic shape once they are embedded in the aerogel, since they are randomly oriented within the silica matrix and no self-assembly on the XRD sample holder can occur. Therefore, in order to understand whether the cubic shape of the dispersed ceria nanoparticles is retained in the as-synthesized and in the thermally treated aerogel nanocomposites, a detailed structural and morphological study has been performed using HAADF-HRSTEM imaging [69].

Following the results already obtained by XRD, the distribution and morphology of the ceria NCs in the SiO<sub>2</sub> matrix has been studied. The large difference in atomic number between Ce and Si provides a high Z-contrast and makes HAADF-HRSTEM the most suitable technique for direct imaging of the ceria NCs embedded in the silica aerogel. This has been carried out on the aerogel nanocomposites as-synthesized and subjected to temperature treatments at 450 °C and at 900 °C, to confirm the effect of supercritical drying and further thermal treatments on the NCs.

The results are presented in Fig. 3 for the 2 wt% aerogel nanocomposite, where the ceria NCs are clearly visible in all conditions (Fig. 3A–C). The 6 wt% aerogel was also investigated (see Fig. S4) but in this case the Ceria NCs are less clearly recognizable despite the larger amount of NCs present in the aerogel.

The 2 wt% aerogel nanocomposite was found to be suitable for a more detailed characterization of the structural features, since a

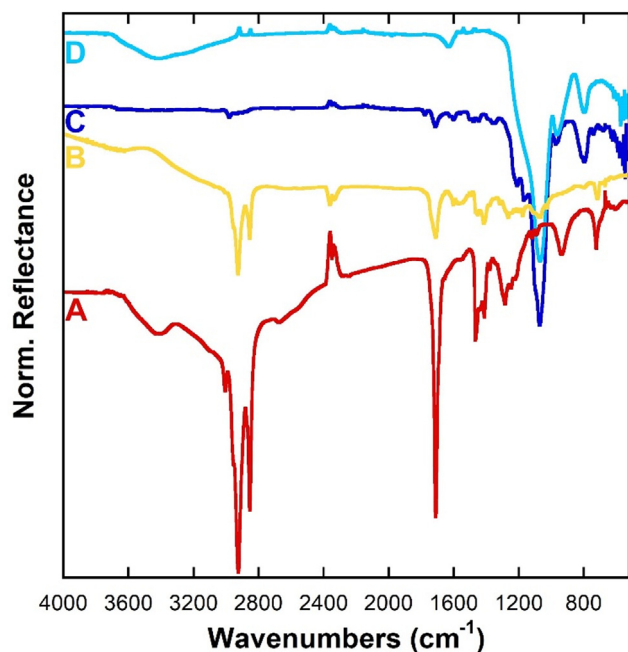


**Fig. 2.** FTIR spectra of: (A) oleic acid, (B) ceria NCs, 2 wt% aerogel nanocomposite as-synthesized (C), and thermally treated at 450 °C (D).

well-dispersed and clearly visible population of NCs is present. The structural characterization of individual ceria NCs within the 2 wt% aerogel nanocomposite can be therefore performed by  $C_s$ -corrected HRSTEM imaging performed in HAADF geometry, even though they are embedded in the silica matrix.

The interplanar distances and the orientation of lattice spacings in the as-synthesized NCs are in agreement with the formation of single crystals of ceria (see Fig. 3D). This same condition is maintained throughout the treatments at 450 °C and 900 °C (shown in Fig. 3E–F), where the typical lattice spacings of ceria can still be identified. Also, HRSTEM imaging confirms the expected preferential faceting in the formation of ceria NCs, with the facets corresponding to the {200} lattice planes, clearly visible in Fig. 3D, E, showing NCs oriented along the [001] zone axis. A slight rounding/truncation at the edges of the NCs, which is typical of ceria NCs [70], can be observed after thermal treatment at 900 °C. Thus, the silica aerogel matrix proves to be able to preserve not only the size but also the cubic shape of the embedded ceria nanoparticles even after the complete removal of oleic acid at 450 °C. Finally, it should be pointed out that when as-synthesized unsupported capped  $CeO_2$  NCs are deposited on a TEM grid from a dispersion in toluene, they self-assemble during the evaporation of the solvent, allowing one to see the square edges of the NCs, as clearly observed in the low magnification TEM imaging shown in Fig. 1A. On the other hand, when the NCs are embedded in the aerogel such self-assembly cannot occur and their images do not

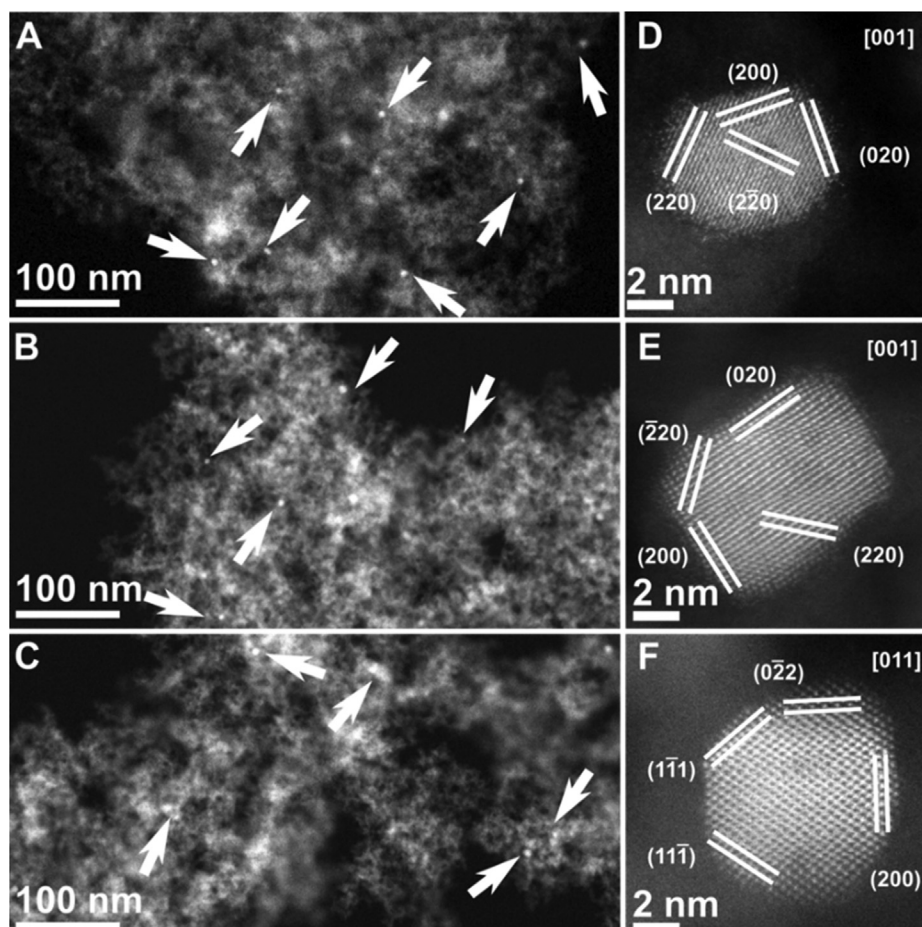


**Fig. 3.** HAADF-STEM image of the 2 wt%  $CeO_2$ - $SiO_2$  aerogel nanocomposites: (A) as-synthesized, (B) after thermal treatment at 450 °C, (C) after thermal treatment at 900 °C. The  $CeO_2$  NCs correspond to the brighter spots within the  $SiO_2$  aerogel matrix and are indicated by arrows.  $C_s$ -corrected HAADF-HRSTEM images showing representative  $CeO_2$  NCs inside the  $SiO_2$  matrix for the 2 wt% aerogel nanocomposites: (D) as-synthesized, (E) after thermal treatment at 450 °C, and (F) after thermal treatment at 900 °C. Images (D–F) highlight the single crystalline nature of the  $CeO_2$  NCs. The relevant zone axes and lattice spaces are indicated in each panel.

show the same square edges, as in the case of the NC displayed in Fig. 3F.

The results presented so far clearly indicate that ceria NCs are stabilized when homogeneously embedded in the silica aerogel. In order to prove that this is accompanied by an easy accessibility to the NC surfaces, HERFD-XANES spectra were collected at the Ce L<sub>3</sub>-edge/L $\alpha$ -line using a Johann-type XES spectrometer [71] while performing *in situ* reduction and oxidation cycles at increasing temperatures. These experiments were performed on the 6 wt% aerogel nanocomposite to achieve a good signal to noise ratio at the Ce L<sub>3</sub>-edge.

The HERFD-XANES technique has excellent ability to probe oxidation state of Ce. Indeed, HERFD-XANES produces better energy resolution spectra [72] than conventional XANES, showing not only the shift in the edge and the modification of the Ce L<sub>3</sub> edge white line, which conventional XANES would display, but also striking changes in the pre- and post-edge features, which are not resolved in conventional XANES spectra. In Fig. 4A, the spectra of CeO<sub>2</sub> (used as Ce<sup>4+</sup> standard) and Ce(NO<sub>3</sub>)<sub>3</sub>·6H<sub>2</sub>O (used as Ce<sup>3+</sup> standard) reference compounds are shown. Prominent differences are observed in the HERFD-XANES spectra of the Ce<sup>3+</sup> and Ce<sup>4+</sup> reference compounds: a significant shift (~5 eV) in the position of the edge is observed with increasing the oxidation state from 3+ to 4+, and is accompanied by changes in both the pre- and post-edge features. Indeed, in the pre-edge region, there is a peak in the Ce<sup>3+</sup> reference compound centred around 5718 eV which is absent in the Ce<sup>4+</sup> reference compound. On the other hand, a prominent peak centred around 5721 eV is present in the Ce<sup>4+</sup> reference compound, with the Ce<sup>3+</sup> reference compound showing just a weak shoulder in this region. In the post-edge, a very intense and broad white line is present only in the Ce<sup>3+</sup> reference compound, while the post-edge features at higher energy are stronger in the Ce<sup>4+</sup> reference compound. All these differences in features greatly enhance the ability to follow the changes in the oxidation state *in situ* and thus to directly measure ceria reactivity. In Fig. 4B, the spectra of the 6 wt% aerogel nanocomposite submitted to reduction/oxidation cycles are shown. All the spectra are typical of samples with a large amount of Ce<sup>4+</sup>, as expected for ceria. However, the changes in the edge position, and in the pre- and post-edge features, do indicate that some Ce<sup>3+</sup> is variably present due to the formation of oxygen vacancies. The spectrum obtained after oxidizing the sample at 275 °C is representative of a sample of almost fully oxidised ceria, with results of the linear combination fitting of the spectrum indicating that only 7% of Ce is present as Ce<sup>3+</sup>, which corresponds to just 1.75% of oxygen vacancies (calculated over the total amount of oxygen atoms in stoichiometric CeO<sub>2</sub>). When the sample is subjected to a reduction treatment at the same temperature, changes occur and linear combination fitting indicates that the Ce<sup>3+</sup> content increases significantly to 27%, and oxygen vacancies to 6.75%. This demonstrates that the redox process is reversible. Further changes are observed by increasing the temperature of the reduction treatment to 400 °C, with the amount of Ce<sup>3+</sup> increasing to 39%, which corresponds to a 9.75% of oxygen vacancies. All of these results indicate that the surface of the NCs is very rich in vacancies, enabling the reversibility of the redox cycle.

Conversely, when the NCs are not embedded in the silica aerogel their reactivity declines dramatically already when performing a reduction and oxidation cycle at 275 °C. In fact, the spectra of unsupported NCs which were collected under oxidising conditions at 275 °C over a period of time indicate a slow progressive oxidation to Ce<sup>4+</sup> (Fig. S5A). After 100 min the spectra do not show further changes, and linear combination fitting indicates 4% of Ce is present as Ce<sup>3+</sup>, i.e. almost fully oxidised. Once the oxidation cycle is completed and a reduction cycle is started no significant changes in the spectra are observed (Fig. S5B), with only a minor increase of Ce<sup>3+</sup> to 7%, indicating that the oxidation of the unsupported NCs is

irreversible. This is due to the slow gradual degradation of the oleic acid used in the synthesis to control their growth, which under oxidising conditions is already degrading at such low temperature [63]. Once the oleic acid is degraded, coalescence and growth occur, accompanied by a dramatic reduction of surface area where the vacancies can be located. As a consequence, when the sample is completely oxidized to Ce<sup>4+</sup> it cannot be reduced back to Ce<sup>3+</sup>. By embedding the ceria NCs in the silica aerogels, the oleic acid is also slowly eliminated via the same degradation process occurring at 275 °C under oxidising conditions, but the NCs will not agglomerate and grow. Thus, due to the presence of the highly porous matrix, both the NCs cubic shape and the shape-related reactivity are preserved, with the redox cycle being reversible.

The approach developed in this work will help to overcome the challenges of using high quality NCs, that can be prepared by surfactant-assisted high temperature solution routes (i.e. highly crystalline, nearly monodisperse in size and with well-defined morphology), for technological applications. The effectiveness of the proposed approach relies on the ability to disperse the as-synthesized capped NCs within the highly porous matrix of a SiO<sub>2</sub> aerogel, which is achieved during the sol–gel synthesis at the sol production step, in order to ensure effective and homogeneous dispersion.

It should be pointed out that a primary challenge resides in the unfavourable sol–gel environment for the capped ceria NCs. Indeed, oleic acid-capped ceria NCs can be dispersed in non-polar solvents, due to the external non-polar tail of the surfactant, and hence cannot be dispersed in solvents such as ethanol, which are typically used for the sol–gel production of silica aerogels. To overcome such a limitation, we have adapted a sol–gel protocol previously developed by our group [59–61,64,73–75], which has proved to be versatile in the optimization of several synthetic parameters. In particular, the use of urea as the gelation catalyst ensures that gelation times are fast enough to embed the ceria NCs in the silica network despite the polar environment of the sol–gel, while at the same time allowing for a gradual gelation process, as required for the production of a homogeneous aerogel nanocomposite.

Using the synthetic approach detailed in the experimental section, the oleic acid capping the NCs is still present after the supercritical drying and it is removed only under subsequent thermal treatments, after the CeO<sub>2</sub> NCs are successfully embedded in the silica aerogels. This ensures that agglomeration and growth is avoided. Once the aerogel nanocomposites are obtained, the NCs are remarkably thermally stable, allowing optimization of the ceria reactivity.

Aerogels have already been shown to be very effective in keeping nanoparticles apart, avoiding their agglomeration, due to their very extended porous structure and thermal stability [59–61,64,73–75]. In fact, their textural properties undergo very limited changes upon thermal treatment, with most of the porosity being retained up to high temperature. Pore collapse accompanied by crystallization of amorphous silica into dense crystalline quartz only occurs at about 1200 °C [59–61,64,73–75]. Our results demonstrate that these characteristics are key in embedding engineered nanoparticles, such as ceria nanocubes, into the pores of the aerogel.

The produced CeO<sub>2</sub>-SiO<sub>2</sub> aerogels are able to maintain the high reactivity associated to the {100} facets typical of the cubic morphology, as evidenced by the Ce L<sub>3</sub> edge HERFD-XANES results proving that a reversible Ce<sup>3+</sup>/Ce<sup>4+</sup> cycle is achieved. The same technique indicates that when the CeO<sub>2</sub> NCs are not embedded in the silica aerogel, they lose their reactivity already at 275 °C in oxidising conditions *via* a progressive decomposition of the capping agent, followed by agglomeration and growth. It should be noted that the great detail present in the pre- and post-edge features of HERFD-XANES data allows one to rule out not only

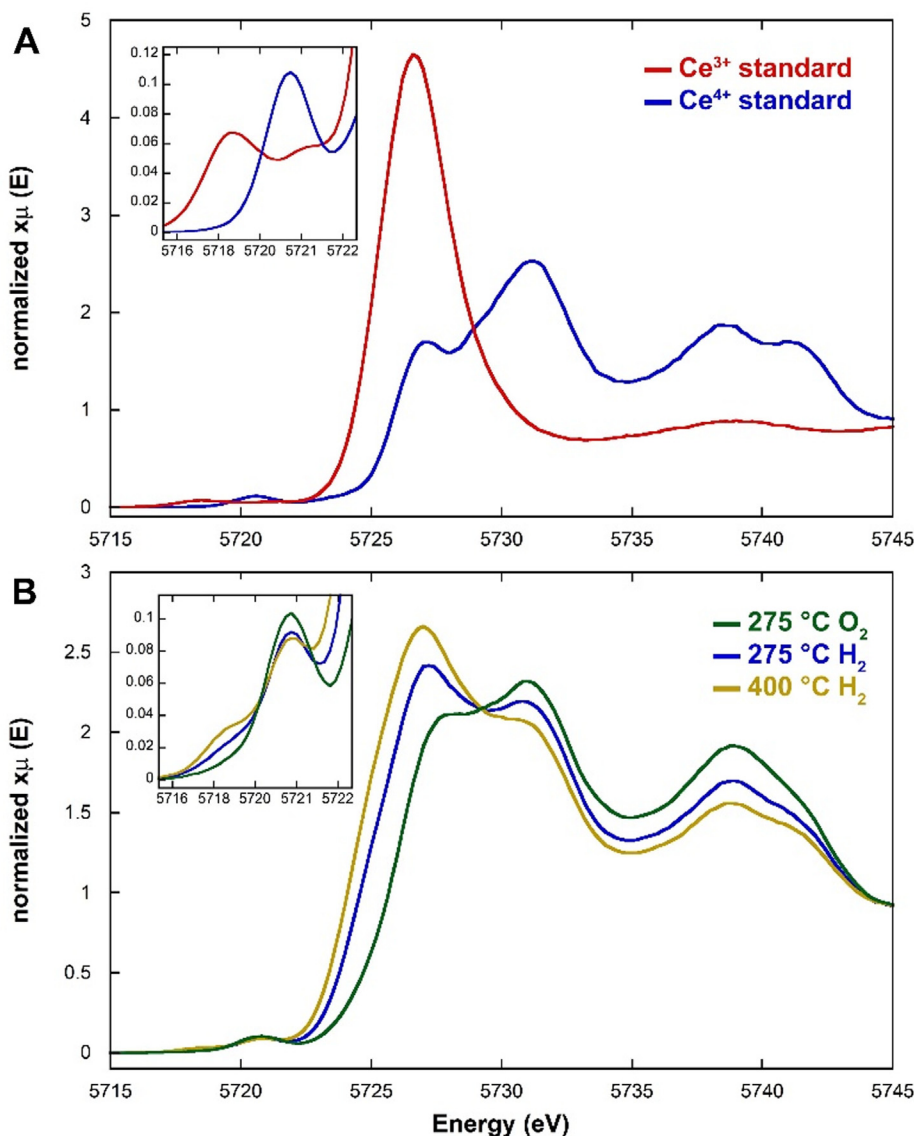


**Fig. 4.** (A) Ce L<sub>3</sub>-edge HERFD-XANES spectra of Ce<sup>3+</sup> and Ce<sup>4+</sup> standards, in energy range of 5715–5745 eV, where the blue trace shows Ce<sup>4+</sup> standard (CeO<sub>2</sub> 99.99% Aldrich) and the red trace shows Ce<sup>3+</sup> standard (Ce(NO<sub>3</sub>)<sub>3</sub>·6H<sub>2</sub>O, 99.99% Aldrich). (B) Ce L<sub>3</sub>-edge HERFD-XANES spectra of the 6 wt% aerogel nanocomposite submitted to an oxidation-reduction cycle at 275 °C, and then a further reduction at 400 °C. The insets show the pre-edge in greater detail. (For interpretation of the references to colour in this figure legend, the reader is referred to the web version of this article.)

the formation of silicates but also interactions between the ceria NCs and the aerogel silica matrix, which would adversely influence the reactivity of the exposed facets. This is because any ceria-silica interaction would modify significantly the pre- and/or post-edge features. Instead, when the samples are submitted to oxidation cycles the observed features are identical to those of the pure CeO<sub>2</sub> standard.

#### 4. Conclusions

Surfactant-free CeO<sub>2</sub> NCs have been successfully embedded in silica aerogels, preserving their shape, and preventing their agglomeration, while the capping agent present on their surface is effectively removed. The obtained aerogel nanocomposites show high reactivity due to the accessibility of highly reactive {100} facets on the surface of the CeO<sub>2</sub> NCs and are remarkably thermally stable.

The current applications of highly engineered shape- and size-controlled nanocrystals, obtained via the surfactant assisted

technique, are limited by their reduced reactivity due to the capping agent on their surface and their poor thermal stability. Instead the aerogel nanocomposites developed in this study can be exploited for important industrial applications, including those requiring high temperatures, opening up new areas of development for highly engineered nanocrystals. The high porosity of silica aerogel is key to maintain accessibility of the ceria NCs and to avoid interactions with the matrix. This represents a significant advance in the field, with respect to previous approaches where surface modifiers are retained in the aerogel [50,51].

It should also be pointed out that the proposed method has the potential to be extended to any surfactant capped nanoparticles, thus allowing one to incorporate highly engineered shape- and size-controlled nanoparticles of different compositions into highly porous silica aerogels, and into aerogels of other compositions, such as alumina. Overall this approach offers an effective solution to the well-known limitations of surfactant-mediated synthesis of NPs for catalytic applications.

## CRediT authorship contribution statement

**Francesco Caddeo:** Conceptualization, Formal analysis, Investigation, Writing - original draft preparation. **Alberto Casu:** Investigation, Formal analysis, Writing - original draft preparation. **Danilo Loche:** Investigation, Formal analysis, Writing - original draft preparation. **Lucy M. Morgan:** Investigation, Formal analysis. **Gavin Mountjoy:** Investigation, Writing - reviewing & editing. **Colm O'Regan:** Investigation, Formal analysis. **Maria F. Casula:** Investigation, Writing - reviewing & editing. **Shusaku Hayama:** Investigation, Methodology. **Anna Corrias:** Conceptualization, Supervision, Writing - reviewing & editing. **Andrea Falqui:** Conceptualization, Supervision, Writing - reviewing & editing.

## Declaration of Competing Interest

The authors declare that they have no known competing financial interests or personal relationships that could have appeared to influence the work reported in this paper.

## Acknowledgements

This work was supported by the British Council UK-Gulf Institutional Links grant (279183790) and by the Engineering and Physical Sciences Research Council (EPSRC) grants (EP/K50306X/1 and EP/1641783). The authors also wish to thank the Diamond Light Source for the award of beam time SP19013. The graphical abstract was produced by Heno Hwang, scientific illustrator at KAUST, who is gratefully acknowledged.

## Appendix A. Supplementary material

Supplementary data to this article can be found online at <https://doi.org/10.1016/j.jcis.2020.09.044>.

## References

- [1] Y. Yin, A.P. Alivisatos, *Nature* 29 (2005) 664–670.
- [2] S.H. Sun, C.B. Murray, D. Weller, L. Folks, A. Moser, *Science* 287 (2000) 1989–1992.
- [3] M.V. Kovalenko, L. Manna, A. Cabot, Z. Hens, D.V. Talapin, C.R. Kagan, V.I. Klimov, A.L. Rogach, P. Reiss, D.J. Milliron, P. Guyot-Sionnest, G. Konstantatos, W.J. Parak, T. Hyeon, B.A. Korgel, C.B. Murray, W. Heiss, *ACS Nano* 9 (2015) 1012–1057.
- [4] C. Wadia, Y. Wu, S. Gul, S.K. Volkman, J. Guo, A.P. Alivisatos, *Chem. Mater.* 21 (2009) 2568–2570.
- [5] V. Cabuil, V. Dupuis, D. Talbot, S. Neveu, *J. Magn. Magn. Mater.* 323 (2011) 1238–1241.
- [6] K. Assaker, C. Carteret, P. Durand, L. Aranda, M.J. Stebé, J.L. Blin, *J. Phys. Chem. C* 117 (2013) 16500–16508.
- [7] T.K. Sau, C.J. Murphy, *J. Am. Chem. Soc.* 126 (2004) 8648–8649.
- [8] P. Pallavicini, A. Donà, A. Casu, G. Chirico, M. Collini, G. Dacarro, A. Falqui, C. Milanese, L. Sironi, A. Taglietti, *Chem. Commun.* 49 (2013) 6265–6267.
- [9] V.F. Puentes, D. Zanchet, C.K. Erdonmez, A.P. Alivisatos, *J. Am. Chem. Soc.* 124 (2002) 12874–12880.
- [10] H. Bin Na, G. Palui, J.T. Rosenberg, X. Ji, S.C. Grant, H. Mattoussi, *ACS Nano* 6 (2012) 389–399.
- [11] X. Peng, L. Manna, W. Yang, J. Wickham, E. Scher, A. Kadavanich, A.P. Alivisatos, *Nature* 2 (2000) 59–61.
- [12] S. Xu, X. Sun, H. Ye, T. You, X. Song, S. Sun, *Mater. Chem. Phys.* 120 (2010) 1–5.
- [13] S. Lentijo-Mozo, D. Deiana, E. Sogne, A. Casu, A. Falqui, *Chem. Mater.* 30 (2018) 8099–8112.
- [14] A. Casu, D. Loche, S. Lentijo-Mozo, A. Falqui, *Molecules* 25 (2020) 1234.
- [15] E. Zuddas, S. Lentijo-Mozo, A. Casu, D. Deiana, A. Falqui, *J. Phys. Chem. C* 121 (2017) 17005.
- [16] A. Heuer-Jungemann, N. Feliu, I. Bakaimi, M. Hamaly, A. Alkilany, I. Chakraborty, A. Masood, M.F. Casula, A. Kostopoulou, E. Oh, K. Susumu, M.H. Stewart, I.L. Medintz, E. Stratakis, W.J. Parak, A.G. Kanaras, *Chem. Rev.* 119 (2019) 4819–4880.
- [17] S. Campisi, C.E. Chan-Thaw, D. Wang, A. Villa, L. Prati, *Catal. Today* 278 (2016) 91–96.
- [18] D. Li, C. Wang, D. Tripkovic, S. Sun, N.M. Markovic, V.R. Stamenkovic, *ACS Catal.* 2 (2012) 1358–1362.
- [19] M. Cargnello, *Chem. Mater.* 31 (2019) 576–596.
- [20] M. Cargnello, C. Chen, B.T. Diroll, V.V. Doan-Nguyen, R.J. Gorte, C.B. Murray, *J. Am. Chem. Soc.* 137 (2015) 6906–6911.
- [21] E. Casals, M.F. Gusta, J. Piella, G. Casals, W. Jiménez, V. Puentes, *Front. Immunol.* 8 (2017) 970.
- [22] L. Falchi, L. Bogliolo, G. Galleri, F. Ariu, M.T. Zedda, A. Pinna, L. Malfatti, P. Innocenzi, S. Ledda, *Theriogenology* 85 (2016) 1274–1281.
- [23] X. Sun, Y. Jian, H. Wang, S. Ge, M. Yan, J. Yu, *ACS Appl. Mater. Interfaces* 11 (2019) 16198–16206.
- [24] T. Montini, M. Melchionna, M. Monai, P. Fornasiero, *Chem. Rev.* 116 (2016) 5987–6041.
- [25] Y. Liu, T. Hayakawa, K. Suzuki, S. Hamakawa, T. Tsunoda, T. Ishii, M. Kumagai, *Appl. Catal. A: Gen.* 223 (2002) 137–145.
- [26] F. Yang, J. Graciani, J. Evans, P. Liu, J. Hrbek, J.F. Sanz, J.A. Rodriguez, *J. Am. Chem. Soc.* 133 (2011) 3444–3451.
- [27] Y.Q. Su, I.A. Filot, J.X. Liu, E.J. Hensen, *ACS Catal.* 8 (2018) 75–80.
- [28] P. Sudarsanam, B. Hillary, M.H. Amin, N. Rockstroh, U. Bentrup, A. Brückner, S. K. Bhargava, *Langmuir* 34 (2018) 2663–2673.
- [29] W. Zhang, X. Niu, L. Chen, F. Yuan, Y. Zhu, *Sci. Rep.* 6 (2016) 29062.
- [30] C.D. Curran, L. Lu, C.J. Kiely, S. McIntosh, *J. Mater. Chem. A* 6 (2018) 244–255.
- [31] A. Kubacka, A. Martínez-Arias, M. Fernández-García, *ChemCatChem* 7 (2015) 3614–3624.
- [32] D. Carta, T. Montini, M.F. Casula, M. Monai, S. Bullita, P. Fornasiero, A. Corrias, *J. Mater. Chem. A* 5 (2017) 20024–20034.
- [33] S. Zhang, Z.Q. Huang, Y. Ma, W. Gao, J. Li, F. Cao, L. Li, C.-L. Chng, Y. Qu, *Nat. Commun.* 8 (2017) 15266.
- [34] C. Riley, S. Zhou, D. Kunwar, A. De La Riva, E. Peterson, R. Payne, L. Gao, S. Lin, H. Guo, A. Datye, *J. Am. Chem. Soc.* 140 (2018) 12964–12973.
- [35] L. Wang, Y. Yu, H. He, Y. Zhang, X. Qin, B. Wang, *Sci. Rep.* 7 (2017) 12845.
- [36] N.V. Skorodumova, S.I. Simak, B.I. Lundqvist, I.A. Abrikosov, B. Johansson, *Phys. Rev. Lett.* 89 (2002) 166601.
- [37] J. Li, X. Liu, W. Zhan, Y. Guo, Y. Guo, G. Lu, *Catal. Sci. Tech.* 6 (2016) 897–907.
- [38] N.J. Lawrence, J.R. Brewer, L. Wang, T.S. Wu, J. Wells-Kingsbury, M.M. Ihrig, G. Wang, Y.-L. Soo, W.-N. Mei, C.L. Cheung, *Nano Lett.* 11 (2011) 2666–2671.
- [39] M. Nolan, S. Grigoleit, D.C. Sayle, S.C. Parker, G.W. Watson, *Surf. Sci.* 576 (2005) 217–229.
- [40] J. Paier, C. Penschke, J. Sauer, *Chem. Rev.* 113 (2013) 3949–3985.
- [41] A. Trovarelli, J. Llorca, *ACS Catal.* 7 (2017) 4716–4735.
- [42] J. Zhang, H. Kumagai, K. Yamamura, S. Ohara, S. Takami, A. Morikawa, H. Shinjoh, K. Kaneko, T. Adschiri, A. Suda, *Nano Lett.* 11 (2011) 361–364.
- [43] H.X. Mai, L.D. Sun, Y.W. Zhang, R. Si, W. Feng, H.P. Zhang, H.-C. Liu, C.-H. Yan, *J. Phys. Chem. B* 109 (2005) 24380–24385.
- [44] X. Wang, Z. Jiang, B. Zheng, Z. Xie, L. Zheng, *CrystEngComm* 14 (2012) 7579–7582.
- [45] J. Zhang, S. Ohara, M. Umetsu, T. Naka, Y. Hatakeyama, T. Adschiri, *Adv. Mater.* 19 (2007) 203–206.
- [46] S. Yang, L. Gao, *J. Am. Chem. Soc.* 128 (2006) 9330–9331.
- [47] T.X. Sayle, F. Caddeo, X. Zhang, T. Sakthivel, S. Das, S. Seal, S. Ptasińska, D.C. Sayle, *Chem. Mater.* 28 (2016) 7287–7295.
- [48] A. Migani, G.N. Vayssilov, S.T. Bromley, F. Illas, K.M. Neyman, *J. Mater. Chem.* 20 (2010) 10535–10546.
- [49] X.D. Zhou, W. Huebner, *App. Phys. Lett.* 79 (2001) 3512–3514.
- [50] T. Berestok, P. Guardia, J. Blanco, R. Nafria, P. Torruella, L. López-Conesa, S. Estradé, M. Ibáñez, J. de Roo, Z. Luo, D. Cadavid, J.C. Martins, M.V. Kovalenko, F. Peiró, A. Cabot, *Chem. Mater.* 29 (2017) 4418–4424.
- [51] T. Berestok, P. Guardia, R. Du, J. Blanco Portals, M. Colombo, S. Estradé, F. Peiró, S.L. Brock, A. Cabot, *ACS Appl. Mater. Interfaces* 10 (2018) 16041–16048.
- [52] A.S. Dorcheh, M.H. Abbasi, *J. Mater. Process. Tech.* 199 (2008) 10–26.
- [53] W. Wan, R. Zhang, M. Ma, Y. Zhou, *J. Mater. Chem. A* 6 (2018) 754–775.
- [54] W. Malfait, S. Zhao, R. Verel, S. Iswar, D. Rentsch, R. Fener, Y. Zhang, B. Milow, M.M. Koebel, *Chem. Mater.* 27 (2015) 6737–6745.
- [55] D. Loche, L. Malfatti, D. Carboni, V. Alzari, A. Mariani, M.F. Casula, *RSC Adv.* 6 (2016) 66516–66523.
- [56] M. Alnaief, S. Antonyuk, C.M. Hentzschel, C.S. Leopold, S. Heinrich, I.A. Smirnova, *Microp. Mesop. Mater.* 160 (2012) 167–173.
- [57] A. Lamy-Mendes, R.F. Silva, L. Durães, *J. Mater. Chem. A* 6 (2018) 1340–1369.
- [58] P.J. Yu, M.H. Lee, H.M. Hsu, H.M. Tsai, Y.W. Chen-Yang, *RSC Adv.* 5 (2015) 13985–13992.
- [59] L. Vanyorek, D. Loche, H. Katona, M.F. Casula, A. Corrias, Z. Kónya, A. Kukovec, I. Kiricsi, *J. Phys. Chem. C* 115 (2011) 5894–5902.
- [60] D. Loche, M.F. Casula, A. Corrias, S. Marras, P. Moggi, *Catal. Lett.* 142 (2012) 1061–1066.
- [61] S. Marras, D. Loche, D. Carta, M.F. Casula, M. Schirru, M.G. Cutrufello, A. Corrias, *ChemPlusChem* 81 (2016) 421–432.
- [62] G.M. Pajonk, *Appl. Catal.* 72 (1991) 217–266.
- [63] D. Loche, L.M. Morgan, A. Casu, G. Mountjoy, C. O'Regan, A. Corrias, A. Falqui, *RSC Adv.* 9 (2019) 6745–6751.
- [64] M.F. Casula, D. Loche, S. Marras, G. Paschina, A. Corrias, *Langmuir* 23 (2007) 3509–3512.
- [65] D. Loche, M.F. Casula, A. Falqui, S. Marras, A. Corrias, *J. Nanosci. Nanotechnol.* 10 (2010) 1008–1016.
- [66] B. Ravel, M. Newville, *J. Synchrotron Radiat.* 12 (2005) 537–541.
- [67] PDF-2 File, ICDD International Centre for Diffraction Data, 1601 Park Lane, Swarthmore, USA, card 34-0394.
- [68] E. Rocchini, A. Trovarelli, J. Llorca, G.W. Graham, W.H. Weber, M. Maciejewski, A. Baikerx, *J. Catal.* 194 (2000) 461–478.

- [69] R. Erni, *Aberration-Corrected Imaging in Transmission Electron Microscopy*, 2nd Ed., Imperial College Press, London, 2015.
- [70] U. Castanet, C. Feral-Martin, A. Demourgues, R.L. Neale, D.C. Sayle, F. Caddeo, J. M. Flitcroft, R. Caygill, B.J. Poynton, M. Molinari, J. Majimel, *ACS Appl. Mater. Interfaces* 11 (2019) 11384–11390.
- [71] S. Diaz-Moreno, M. Amboage, M. Basham, R. Boada, N.E. Bricknell, G. Cibir, T. M. Cobb, J. Filik, A. Freeman, K. Geraki, D. Gianolio, S. Hayama, K. Ignatyev, L. Keenan, I. Mikulska, J.F.W. Mosselmans, J.J. Mudd, S.A. Parry, *J. Synchrotron Radiat.* 25 (2018) 998–1009.
- [72] K. Hamalainen, D.P. Siddons, J.B. Hastings, L.E. Berman, *Phys. Rev. Lett.* 67 (1991) 2850.
- [73] A. Casu, M.F. Casula, A. Corrias, A. Falqui, D. Loche, S. Marras, C. Sangregorio, *Phys. Chem. Chem. Phys.* 10 (2008) 1043–1052.
- [74] A. Casu, M.F. Casula, A. Corrias, A. Falqui, D. Loche, S. Marras, *J. Phys. Chem. C* 111 (2007) 916–922.
- [75] D. Carta, M.F. Casula, A. Falqui, D. Loche, G. Mountjoy, C. Sangregorio, A. Corrias, *J. Chem. Phys. C* 113 (2009) 8606–8615.